Editors' Suggestion

Phonon-Assisted Broadband Light Emission in Strain-Gradient-Modulated Diamond Nanoribbons

Yuxuan Zhang,[1,*] Shuo Qiao,[1,*] Anliang Lu,[2,*] Xiaohui Sun,[1] Jun Lyu,[1] Jinlong Du,[3,§] Yang Lu,[2,‡] and Lin Yang[1,4,†]

[1]School of Advanced Manufacturing and Robotics, Peking University, Beijing 100871, People's Republic of China
[2]Department of Mechanical Engineering, The University of Hong Kong, Hong Kong, People's Republic of China
[3]Electron Microscopy Laboratory, School of Physics, Peking University, Beijing 100871, People's Republic of China
[4]National Key Laboratory of Advanced Micro and Nano Manufacture Technology, Peking University, Beijing 100871, China

(Received 5 February 2026; revised 8 June 2026; accepted 31 July 2026; published 3 September 2026)

Diamond offers an exceptional platform for optoelectronics owing to its ultra-wide band gap, superior thermal and photonic properties. Yet its optical response is notoriously difficult to tune, as conventional doping suffers from deep impurity levels and poor activation efficiency. Here, we show that strain-gradient engineering provides a doping-free route to modulate broadband optical emission in microfabricated diamond. By taking advantage of size-induced large elasticity, we show that controlled elastic bending of diamond nanoribbons generates spatially varying strain fields that can be resolved at nanoscale using STEM-EELS, which reveals synchronous electronic bandgap shifts and phonon spectrum broadening. Spatially mapped cathodoluminescence exhibits continuous emission shifts, accompanied by intensity variations and spectral widening. Theoretical analyses show that nonuniform strain couples electronic band restructuring with phonon mode redistribution, expanding the pathways for phonon-assisted optical transitions. These findings transform diamond from a static wide-band-gap semiconductor into a mechanically reconfigurable broadband emitter, establishing strain-gradient engineering as a general paradigm for tunable photonics in wide-band-gap semiconductors.

DOI: 10.1103/gcf5-chmf

Introduction—Diamond is an ultrawide band gap semiconductor with exceptional carrier mobility [1], outstanding thermal conductivity [2], deep-ultraviolet emission [3], and stable single-photon emission [4], making it a compelling platform for next-generation microelectronic and optoelectronic technologies [5,6]. Yet its electronic and optical properties are difficult to tune: conventional doping introduces deep impurity levels with low activation efficiency and limited solubility, constraining the realization of integrated functional devices [7]. Elastic strain engineering has recently emerged as a promising alternative [8,9]. Advances in microfabrication have enabled ultra-large elastic strains realized in diamond micro- or nanostructures (up to ∼10%, approaching theoretical limit) [10–12], allowing continuous and reversible electronic bandgap modulation, driving transitions from insulating to semiconducting, metallic, and even superconducting behavior [13,14]. This establishes a route toward mechanically reconfigurable diamond photonics [3,15]. However, the experimental implementation of strain-based optical modulation remains in its infancy, hindered by the difficulty of precisely controlling nanoscale strain fields and the complex interplay of phonon-assisted light emission in an indirect band gap system.

Here, we introduce strain-gradient-engineered diamond nanoribbons, where controlled bending creates spatially varying strain that enables broadband light emission and detection within a single material system—eliminating the need for multilayer or multi-band-gap heterostructures [16,17]. As an indirect band gap material, diamond requires phonon-assisted optical transitions to satisfy momentum conservation due to the k-space offset between its conduction band minimum and valence band maximum [18,19]. A strain gradient modifies these transitions through two cooperative mechanisms: (i) tensile or compressive strains alter the phonon density of states, changing the population of excited phonons at a given temperature and consequently modulating luminescence intensity, and (ii) strain-gradient-induced phonon spectrum broadening expands the available momentum-matching pathways and thereby widens the emission spectrum. Collectively, unlike conventional uniform strain engineering that primarily shifts electronic bands, strain gradients continuously reconstruct the phonon energy–momentum landscape governing indirect optical processes, opening additional pathways for phonon-assisted light emission.

*These authors contributed equally to this work.
†Contact author: linyangpku@pku.edu.cn
‡Contact author: ylu1@hku.hk
§Contact author: jldu@pku.edu.cn

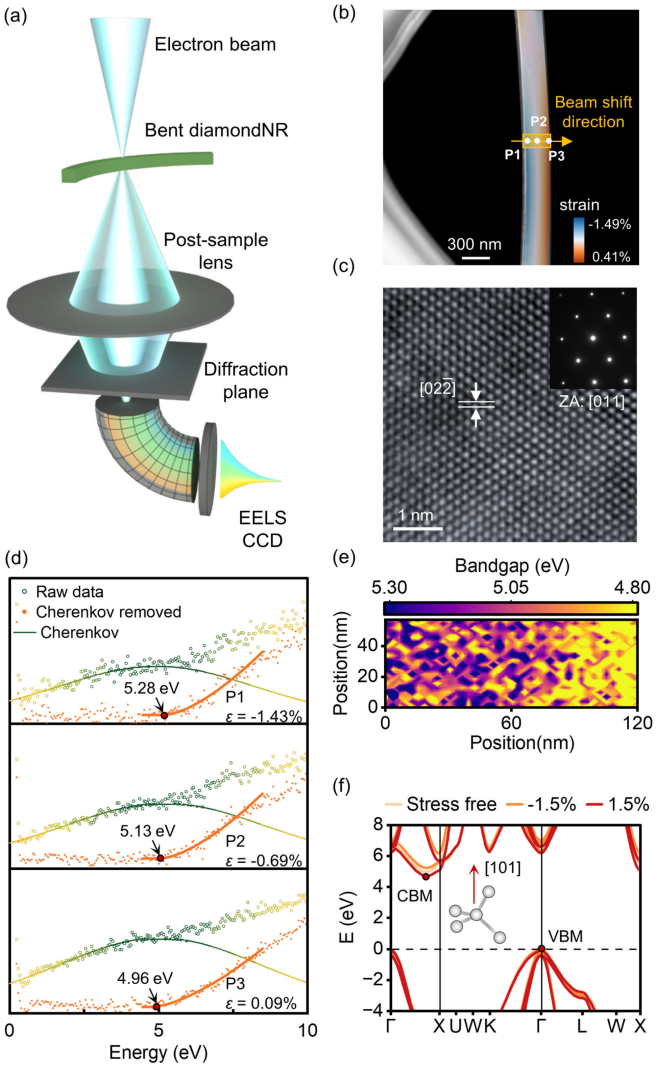

FIG. 1. EELS characterization and theoretical simulation of electronic band gap modulation in bent diamond nanoribbons. (a) Schematic of the experimental setup (EELS) to simultaneously acquire electronic band gap and local lattice vibrational spectra. (b) SEM image of bent diamond nanoribbon and the calculated strain contour is overlaid on top. (c) High-resolution TEM image shows the lattice of a diamond nanoribbon, where the arrow indicates that the ribbon is microfabricated along the [011] direction. (d) EELS low loss signal showing the electronic band gap measurements at location P1, P2, and P3 marked in panel (b), the orange-green gradient points represent the measured raw data, where the color gradient denotes the relative Cherenkov loss, with greener points indicating a larger contribution. The green-shaded curve corresponds to the fitted Cherenkov loss. The orange points and the corresponding orange curve represent the Cherenkov-corrected data and the fitting result, respectively. (e) Electronic band gap mapping along the beam shift direction of the bent diamond nanoribbons [yellow region in panel (b)]. (f) First-principles calculated band structure of bent diamond nanoribbons under [110]-directional strain in the first Brillouin zone.

In this Letter, we microfabricated single-crystalline diamond nanoribbons and introduced well-defined strain gradients through controlled bending. To directly visualize the resulting modifications to the electronic and vibrational band structure, we performed atomically resolved scanning transmission electron microscopy electron energy loss spectroscopy [STEM-EELS, Fig. 1(a)], which enables simultaneous mapping of local bandgap energies and lattice vibrational modes. These measurements reveal continuous bandgap modulation and systematic phonon peak shifts across the strain gradient, in agreement with first-principles calculations. Spatially resolved cathodoluminescence further shows position-dependent emission energies, accompanied by modulated luminescence intensity and pronounced spectral broadening, providing direct evidence that strain gradients enable broadband optical response in diamond. Beyond diamond, this work provides a general framework for mechanically programmable broadband photonics, with potential implications for adaptive optoelectronics, strain-engineered quantum emitters, and reconfigurable photonic systems.

Electronic band gap evolution under bending—Single-crystalline, undoped diamond synthesized via chemical vapor deposition [20,21] was patterned into nanoribbons using focused ion beam (FIB) milling (Fig. S1 [22]). High-resolution transmission electron microscopy (HRTEM) imaging [Fig. 1(c)] and the corresponding electron diffraction pattern confirm the preserved single-crystal quality. A well-defined strain gradient was introduced by mechanically bending the diamond nanoribbon (DNR) with a microprobe (Fig. S2 [22]), and then fixing both ends to a SiN support grid via localized platinum deposition to prevent stress relaxation [Fig. 1(b)]. The resulting strain distribution in the bent DNR, obtained via finite element analysis [22], is shown in Fig. 1(b). The maximum principal strain, $\epsilon_{\max}$, was determined to be 1.49%, well below the reported elastic limit of diamond [10–12], ensuring that the nanoribbon remains entirely within the elastic deformation regime.

We employed STEM-EELS to probe the local electronic bandgap along the strain gradient in the bent DNR [Fig. 1(a)] [22]. EELS spectra were collected at three distinct positions corresponding to different elastic strain, labeled P1–P3 in Fig. 1(b). To minimize the influence of amorphous carbon, the diamond nanoribbon sample was prepared with amorphous surface layers thinner than ~3 nm on each side, corresponding to less than 4% of the total specimen thickness along the electron-beam direction (Supplemental Material note 1 and Figs. S3, S4 [22]). Note that on-axis EELS measurements in diamond are affected by Cherenkov radiation, which contributes a low-energy background near 5 eV [Fig. 1(d)]. To remove this contribution, we fitted and subtracted the Cherenkov background using a second-order logarithmic

polynomial function prior to band gap extraction. The band gap onset was subsequently determined from the Cherenkov-corrected spectra using $I = \alpha(E - Eg)^{1.5}$ [22,40]. The processed spectra are shown in Fig. 1(d). As the local strain evolves from −1.43% (compressive) to 0.09% (tensile), the extracted electronic bandgap decreases from 5.28 to 4.96 eV.

To improve statistical reliability, EELS spectra were additionally acquired along the beam shift direction within the rectangular region marked in Fig. 1(b), followed by identical data processing workflow to extract the band gap values (Fig. S2 [22]). The resulting two-dimensional band gap map [Fig. 1(e)] shows a pronounced monotonic variation: as the local compressive strain decreases, the band gap decreases from 5.30 to 4.80 eV across a ∼1.90% strain difference. This trend is consistent with the discrete point measurements in Fig. 1(d), and the strain-induced band gap variation aligns well with previous observations in tensile-strained nanodiamond [11]. To further validate the Cherenkov-removal procedure, we performed additional off-axis EELS measurements, in which the Cherenkov feature around 5 eV is largely suppressed (Supplemental Material note 2, Fig. S5 [22]). Consistent with the on-axis results, the extracted band gap exhibits a monotonic decrease as the local strain evolves from compression to tension.

To complement our experimental observations, we performed first-principles calculations [22] to examine the evolution of the electronic band structure of diamond under uniform elastic strain [Fig. 1(f) and Fig. S6 in [22]]. Consistent with the experimental condition, a uniform strain was applied along the [110] crystallographic direction. The calculations reveal that the valence band maximum (VBM) remains near the Γ point with only minor energy variation under strain, while the conduction band minimum (CBM) shifts downward in energy with increasing tensile strain. This leads to a systematic narrowing of the band gap, in quantitative agreement with our STEM-EELS measurements.

Phonon DOS along strain gradient—In indirect band gap semiconductors such as diamond, radiative recombination is intrinsically inefficient due to the momentum mismatch between the conduction band minimum and valence band maximum. Momentum conservation therefore requires the participation of phonons, unlike in direct band gap materials where photon emission can occur without additional momentum exchange [19]. To understand how strain gradients influence this phonon-assisted recombination pathway, we examined the evolution of the local phonon spectra across the bent nanoribbon.

Taking advantage of the meV energy resolution and subnanometer spatial resolution of STEM-EELS, we performed continuous spatial mapping of the local vibrational spectra across the strain gradient in the bent diamond nanoribbons [Fig. 2(a), [22]], followed by multi-peak

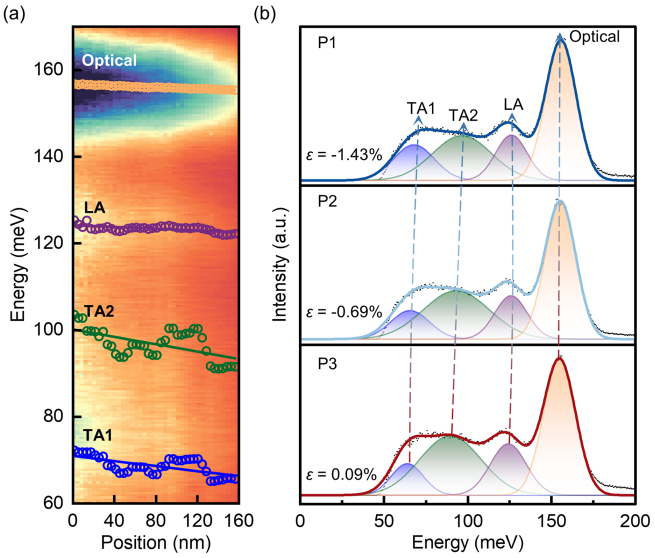

FIG. 2. EELS characterization of phonon DOS in bent diamond nanoribbons. (a) EELS mapping of measured lattice vibrational intensity along the beam shift direction of the bent diamond nanoribbons [yellow region in Fig. R4(b)]. (b) Measured lattice vibrational intensity at P1, P2, and P3, accompanied with Lorentzian fitting of each phonon peak. Arrows mark the energy shift of phonon peaks from tensile to compressive region.

Lorentzian fitting of the acquired spectra [Fig. 2(b)]. The extracted phonon energies are in excellent agreement with reported diamond phonon frequencies in the literature [41,42] (Table S1 [22]). The mapping reveals that, as the local strain varies from −1.43% to 0.09%, the TA1, TA2, LA, and optical modes decrease by ∼4, 7, 2.3, and 1.5 meV, respectively.

The as-acquired vibrational spectra reflect momentum-integrated phonon modes across the entire Brillouin zone and are thus closely related to the projected phonon density of states (DOS). To interpret the experimental findings, we performed molecular dynamics (MD) simulations to calculate the phonon DOS in diamond under strain gradients (Methods and Supplemental Material notes 3 and 4 [22]). As shown in Fig. S9 [22], the calculated DOS exhibits systematic blueshifts in all six characteristic phonon modes as the local strain evolves from tensile to compressive (Table S2 [22]), consistent with the trend observed in the EELS measurements. Quantitatively, the experimentally measured phonon energy shifts agree, within the experimental uncertainty, with the calculated shifts of $\sim 2-3$ meV over the corresponding strain range. As discussed below, this strain-induced redistribution of phonon modes modifies the population of excited phonons at a given temperature, which affects the availability of phonons that participate in momentum-conserving recombination and leads to measurable changes in luminescence intensity in bent diamond nanostructures.

Phonon dispersion broadening effect—Beyond shifting phonon energies, strain gradients can also broaden the

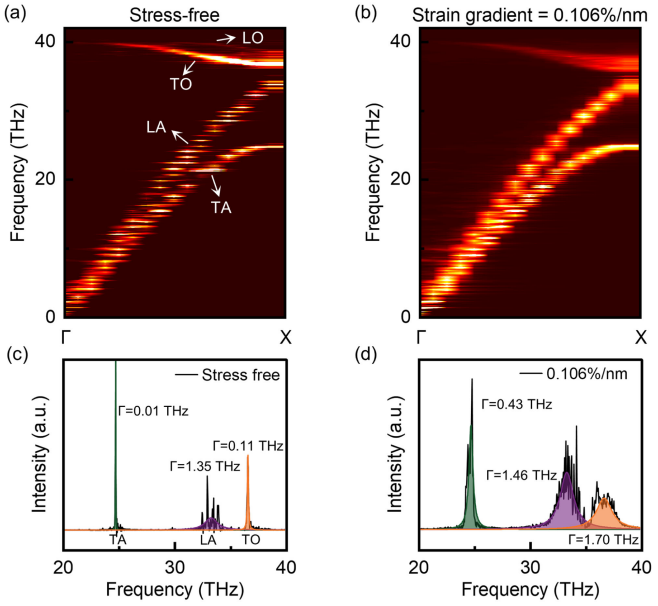

FIG. 3. Phonon dispersion broadening in bent diamond nanoribbons under different strain gradient. (a),(b) Calculated phonon dispersions under strain gradient of (a) stress free, (b) 0.106%/nm. (c),(d) Slices of phonon dispersions under different strain gradients at wave vector $k = [0, 1.76, 0]$ Å^{-1}, along the Γ-X direction of the diamond Brillouin zone. The colored curves are Lorentzian-fitted phonon peaks, which show a pronounced broadening effect as the strain gradient increases.

phonon spectrum, which has a pronounced impact on luminescence by modifying the energy–momentum availability for phonon-assisted radiative recombination. To examine this broadening effect, we combined first-principles calculations with MD simulations to evaluate the evolution of phonon dispersion under varying strain gradients (Methods and Supplemental Material note 5 [22]). The calculated phonon dispersion of unstrained diamond is shown in Fig. 3(a), where the transverse acoustic (TA), longitudinal acoustic (LA), transverse optical (TO), and longitudinal optical (LO) branches are clearly resolved. As the strain gradient increases [Figs. 3(a), 3(b), and Fig. S10], the phonon branches progressively broaden, indicating a widening of the vibrational state distribution at a given momentum [43].

In the stress-free case, phonon frequencies at a given wave vector k are sharply defined, reflecting a uniform lattice and well-defined interatomic force constants [44]. In contrast, when a strain gradient is introduced, as in bent nanoribbons, spatially varying interatomic distances perturb the local force constants F [43]. In real space, this leads to local variations in phonon frequencies along the strain gradient. When transformed into momentum space, these local fluctuations manifest as a broadening of the phonon frequency distribution at each wave vector. This effect is clearly observed in Figs. 3(a), 3(b), and Fig. S10, where the phonon branches progressively widen with increasing strain gradients.

To directly reveal the phonon spectrum broadening induced by strain gradients, we extracted the intensity–ω profiles along the $k = [0, 1.76, 0]$ Å^{-1} direction and quantified the phonon linewidths through fitting the spectral peaks with Lorentzian functions [45] [Figs. 3(c) and 3(d)]. As the strain gradient increases from 0 to 0.106%/nm, the linewidths of the TA, LA, and TO modes expand to ∼43, ∼1.08, and ∼15-fold of their original (stress-free) values, respectively. A further increase in the strain gradient leads to a more significant broadening effect. Similar strain gradient-induced phonon spectrum broadening was first reported in Si nanoribbons [43], and has since been observed in other materials, including bent BAs nanoribbons [46], and bent van der Waals materials [47]. From an optoelectronic perspective, the broadened phonon spectrum diversifies the phonon energy distribution at a given wave vector, enabling a wider range of phonon modes to satisfy momentum conservation in phonon-assisted radiative transitions. This, in turn, expands the set of allowable electronic transitions and thereby widens the emission spectrum.

Phonon-assisted luminescence under strain gradient—To probe the luminescence response under strain gradients, we performed spatially resolved cathodoluminescence (CL) measurements on bent diamond nanoribbons at 80 K [22]. The SEM-CL configuration is schematically illustrated in Fig. 4(a). As the electron beam rastered across the nanoribbon, local band-edge electrons were excited and subsequently relaxed, producing emission spectra that sensitively reflect the local strain state. Variations in peak energy, intensity, and spectral shape therefore provide a direct optical signature of strain-gradient-induced modifications to the luminescence response.

The excitation and emission processes are illustrated in Fig. 4(c). Under high-energy electron irradiation, valence-band electrons are excited to the conduction band via impact ionization. After a series of scattering and relaxation events, carriers recombine radiatively, emitting photons [18]. As diamond is an indirect band gap semiconductor, the momentum mismatch between the conduction band minimum and valence band maximum necessitates phonon participation for momentum conservation. The emitted photon energy is therefore given by $\hbar\nu = E_g - \hbar\omega$, where ν is the photon frequency, E_g is the electronic band gap, ω is the phonon frequency, and $\hbar$ is the reduced Planck constant [48]. For bent nanoribbons under strain gradients, tensile or compressive strains alter the local phonon density of states, thereby modifying phonon populations and modulating luminescence intensity. Moreover, strain-gradient-induced phonon spectrum broadening increases the range of accessible phonon energies under given momentum ($\hbar\Delta\omega$), expanding the set of allowed phonon-assisted transitions as $\hbar\nu = E_g - \hbar(\omega \pm \frac{1}{2}\Delta\omega)$. This, in turn,

broadens the emission energy distribution (i.e., $\hbar\nu$), giving rise to the observed spectral widening.

We collected CL spectra at three representative positions along the nanoribbon, corresponding to distinct local strain states [P1–P3 in Fig. 4(a)]. The spectra exhibited three primary features at ~3.0, ~4.1, and ~5.1 eV (Fig. S10 [22]). Consistent with previous reports [4,49–51], the 3.0 eV "A band" arises from band-tail or defect-related recombination, and the 4.1 eV peak is attributed to nitrogen-related defects in the sample (Supplemental Material note 6 [22]). Since no additional peaks were detected near the intrinsic diamond band gap (5.3 eV) [52] or at higher energies, the 5.1 eV emission is assigned to intrinsic band-edge recombination. Figure 4(b) presents the spectra after subtracting the nitrogen-related contribution, thereby isolating the intrinsic electronic band gap response under strain gradients. As the local strain varies from tensile to compressive (from P1–P3), the intrinsic peak energy, i.e., E_g, shifts from 4.93 to 5.01 eV. This evidences strain-gradient-induced spectral peak shifts and tunable emission in monolithic diamond. The slightly smaller variation observed in the CL peak positions compared with the EELS-derived bandgap evolution [Fig. 1(d)] primarily arises from the substantially larger sampling volume and lower spatial resolution of the CL measurements, which spatially average the local strain-induced band gap variations (Supplemental Material note 7 [22]).

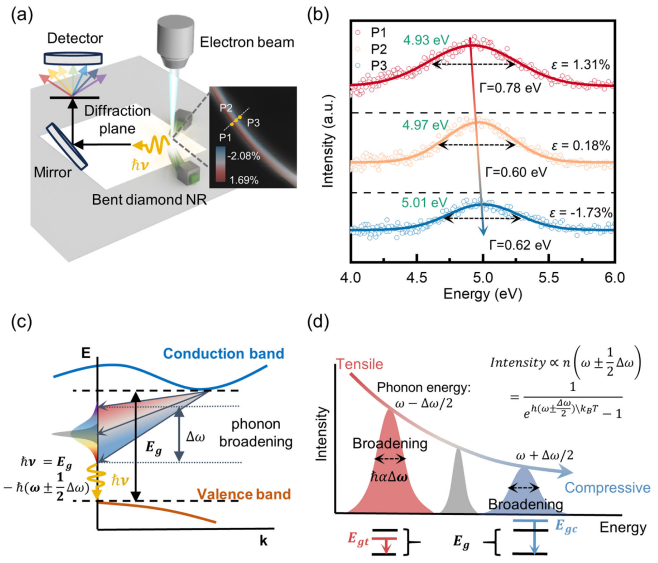

FIG. 4. Cathodoluminescence of bent diamond nanoribbon and phonon-assisted transition processes. (a) Schematic of the experimental setup (CL) and SEM image of the bent diamond nanoribbon, where sampling regions are marked. (b) Measured CL signals showing the distinct emission properties for the three positions (P1–P3) marked in (a). (c) Schematic of phonon-assisted radiative transition in an indirect band gap semiconductor. In the presence of a strain gradient, phonon energies broaden (gradient-colored region), providing a wider set of phonon modes for momentum conservation. (d) The illustration shows how tensile and compressive strain states shift the local emission energy, modulate emission intensity, and alter spectral shape. Tensile and compressive strain modify the electronic band gap (E_{gt}, and E_{gc}), leading to corresponding shifts in the emission peak energy. Changes in phonon energies under strain alter the local phonon occupation, affecting the availability of phonons that assist radiative recombination and thus modulating emission intensity. Under a strain gradient, the phonon spectrum broadens, expanding the range of phonon energies available for momentum-conserving transitions and producing a broadened emission peak ($\hbar\alpha\Delta\omega$).

The influence of strain gradient-modulated phonon-assisted emission is reflected in changes to both the peak intensity and peak width. As shown in Fig. 4(b), the luminescence intensity on the compressive side is lower by 36% compared to that on the tensile side. This behavior can be rationalized by phonon excitation statistics. At the measurement low temperature T of 80 K, the average phonon occupation at frequency ω follows the Bose-Einstein distribution $n(\omega) = 1/(e^{\hbar\omega/k_BT} - 1)$, where $\hbar$ and k_B denote the reduced Planck constant and Boltzmann constant, respectively. Both EELS and MD results (Fig. 2) show that phonon spectra broadening, $\Delta\omega$, leads to phonon frequencies higher in the compressive side $(\omega + \frac{1}{2}\Delta\omega)$ than in the tensile side $(\omega - \frac{1}{2}\Delta\omega)$. Consequently, phonons in the compressive region have lower thermal occupation, reducing the number of phonons available to assist momentum-conserving radiative recombination [Fig. 4(d)]. This reduced phonon participation directly accounts for the observed decrease in luminescence intensity on the compressive side [Fig. 4(b)].

In addition, Fig. 3 demonstrates that the strain gradient induces pronounced phonon spectrum broadening, enriching the phonon energy distribution at a given wave vector. As a result, during phonon-assisted recombination in diamond, the phonons available to satisfy momentum conservation span a continuous range of frequencies rather than a discrete set. This expanded phonon participation widens the energy window of photon emission, giving rise to a luminescence peak significantly broader than that in the strain-gradient-free state, i.e., $\hbar\nu = E_g - \hbar(\omega \pm \frac{1}{2}\Delta\omega)$ [Figs. 4(c) and 4(d)]. Importantly, only phonons associated with strain states within the atomic interaction cutoff radius can contribute locally [43]. Thus, only a fraction α of the broadened phonon spectrum participates in radiative transitions, and the observable spectral broadening is narrower than the full phonon-spectrum broadening, scaling approximately as $\alpha\Delta\omega$ [43]. A comparison with CL spectra from an unstrained nanoribbon further highlights this effect [48,50]. Although the intrinsic emission peak near 5.3 eV is preserved, its full width at half maximum (FWHM) is substantially narrower than that observed under a strain gradient [less than 0.20 eV vs ~0.70 eV; Fig. 4(b)].

Discussion—In this Letter, we used STEM-EELS and CL spectroscopy to reveal how strain gradients modulate the optoelectronic response of diamond nanoribbons. We show that strain gradients simultaneously modulate the

electronic band gap and broaden the phonon spectrum, thereby activating new phonon-assisted radiative pathways. This dual modulation produces systematic shifts in emission energy, intensity redistribution, and pronounced spectral widening. Unlike conventional spectral broadening driven by thermal effect [53] or defect scattering [54], the behavior observed here arises from a geometrically programmed strain field that deterministically reshapes both the electronic and vibrational landscapes. This mechanism enables broadband luminescence in pristine, single-crystal diamond—without alloying, heavy doping, or heterostructure stacking—and establishes strain gradients as a continuously tunable optical control parameter. Beyond demonstrating a direct and reversible link between lattice deformation and photon emission, our results provide a generalizable framework for reconfigurable broadband photonics in wide-band-gap semiconductors, pointing toward a new paradigm of mechanically programmable optoelectronic materials and devices.

Acknowledgments—This work was supported by the National Natural Science Foundation of China (No. 52650008, No. 12588301, No. T2550242, No. 52521007, No. 52476045, and No. 92477139), and Beijing Natural Science Foundation (No. JR26016). We also acknowledge the support from the National Key R&D Program of China (No. 2024YFB4405700). The authors acknowledge Electron Microscopy Laboratory of Peking University, China for the use of Cs corrected Nion U-HERMES200 scanning transmission electron microscopy. A. L. and Y. L. acknowledge the financial support from the National Natural Science Foundation of China under the Type A Grant No. 12525205, and the Research Grants Council of the Hong Kong Special Administrative Region, China, under the Grant No. RFS2021-1S05.

L. Y. proposed and directed the research. A. L. and Y. Z. microfabricated the bent diamond nanoribbons. S. Q. performed EELS measurements with the help from J. D. J. D. performed the off-axis EELS measurements. Y. Z. and S. Q. processed and analyzed the EELS data. Y. Z. conducted first-principles calculation as well as MD simulation. J. D. conducted CL measurements. Y. Z. processed and analyzed the CL data. The manuscript was prepared by L. Y., Y. Z., S. Q., Y. L., and A. L. with input from all co-authors.

The authors declare no competing interests.

Data availability—The data supporting the findings of this study are publicly available [55].

[1] J. Isberg, J. Hammersberg, E. Johansson, T. Wikstrom, D. J. Twitchen, A. J. Whitehead, S. E. Coe, and G. A. Scarsbrook, High carrier mobility in single-crystal plasma-deposited diamond, Science **297**, 1670 (2002).

[2] J. R. Olson, R. O. Pohl, J. W. Vandersande, A. Zoltan, T. R. Anthony, and W. F. Banholzer, Thermal conductivity of diamond between 170 and 1200 K and the isotope effect, Phys. Rev. B **47**, 14850 (1993).

[3] I. Aharonovich and E. Neu, Diamond nanophotonics, Adv. Opt. Mater. **2**, 911 (2014).

[4] R. Schirhagl, K. Chang, M. Loretz, and C. L. Degen, Nitrogen-vacancy centers in diamond: nanoscale sensors for physics and biology, Annu. Rev. Phys. Chem. **65**, 83 (2014).

[5] P. W. May, Materials science. The new diamond age?, Science **319**, 1490 (2008).

[6] I. Aharonovich, A. D. Greentree, and S. Prawer, Diamond photonics, Nat. Photonics **5**, 397 (2011).

[7] A. Lu, L. Yang, C. Dang, H. Wang, Y. Zhang, X. Li, H. Zhang, and Y. Lu, Tuning diamond electronic properties for functional device applications, Functional Diamond **2**, 151 (2022).

[8] C. Dang, A. Lu, H. Wang, H. Zhang, and Y. Lu, Diamond semiconductor and elastic strain engineering, J. Semicond. **43**, 021801 (2022).

[9] W. Liang, L. Yang, J. Zhu, Y. Lian, and Y. Lu, Strain engineering of microfabricated diamond and its applications, APL Mater. **13**, 060602 (2025).

[10] A. Banerjee *et al.*, Ultralarge elastic deformation of nanoscale diamond, Science **360**, 300 (2018).

[11] C. Dang *et al.*, Achieving large uniform tensile elasticity in microfabricated diamond, Science **371**, 76 (2021).

[12] A. Nie *et al.*, Approaching diamond's theoretical elasticity and strength limits, Nat. Commun. **10**, 5533 (2019).

[13] Z. Shi, M. Dao, E. Tsymbalov, A. Shapeev, J. Li, and S. Suresh, Metallization of diamond, Proc. Natl. Acad. Sci. U.S.A. **117**, 24634 (2020).

[14] C. Liu, X. Song, Q. Li, Y. Ma, and C. Chen, Superconductivity in compression-shear deformed diamond, Phys. Rev. Lett. **124**, 147001 (2020).

[15] A. Sipahigil *et al.*, An integrated diamond nanophotonics platform for quantum-optical networks, Science **354**, 847 (2016).

[16] N. Ding *et al.*, A novel approach for designing efficient broadband photodetectors expanding from deep ultraviolet to near infrared, Light Sci. Appl. **11**, 91 (2022).

[17] J. Yao and G. Yang, 2D material broadband photodetectors, Nanoscale **12**, 454 (2020).

[18] C. D. Clark, P. J. Dean, and P. V. Harris, Intrinsic edge absorption in diamond, Proc. R. Soc. A **277**, 312 (1997).

[19] K. Konishi and N. Naka, Phonon-assisted excitonic absorption in diamond, Phys. Rev. B **104**, 125204 (2021).

[20] G. Shu, B. Dai, V. G. Ralchenko, A. P. Bolshakov, A. A. Khomich, E. E. Ashkinazi, J. Han, and J. Zhu, Growth of three-dimensional diamond mosaics by microwave plasma-assisted chemical vapor deposition, CrystEngComm **20**, 198 (2018).

[21] G. Shu *et al.*, Vertical-substrate epitaxial growth of single-crystal diamond by microwave plasma-assisted chemical vapor deposition, J. Cryst. Growth **486**, 104 (2018).

[22] See Supplemental Material at http://link.aps.org/supplemental/10.1103/gcf5-chmf for sample fabrication, experimental and computational methods, sample characterization, and off-axis EELS results, which includes Refs. [23–39].

[23] G. Kresse and J. Furthmüller, Efficiency of ab-initio total energy calculations for metals and semiconductors using a plane-wave basis set, Comput. Mater. Sci. **6**, 15 (1996).
[24] G. Kresse and J. Furthmüller, Efficient iterative schemes for ab initio total-energy calculations using a plane-wave basis set, Phys. Rev. B **54**, 11169 (1996).
[25] P. E. Blochl, O. Jepsen, and O. K. Andersen, Improved tetrahedron method for Brillouin-zone integrations, Phys. Rev. B **49**, 16223 (1994).
[26] J. Sun, R. Haunschild, B. Xiao, I. W. Bulik, G. E. Scuseria, and J. P. Perdew, Semilocal and hybrid meta-generalized gradient approximations based on the understanding of the kinetic-energy-density dependence, J. Chem. Phys. **138**, 044113 (2013).
[27] J. Sun, B. Xiao, and A. Ruzsinszky, Communication: Effect of the orbital-overlap dependence in the meta generalized gradient approximation, J. Chem. Phys. **137**, 051101 (2012).
[28] K. Dabov, A. Foi, V. Katkovnik, and K. Egiazarian, Image denoising by sparse 3-D transform-domain collaborative filtering, IEEE Trans Image Process **16**, 2080 (2007).
[29] M. M. Hall, V. G. Veeraraghavan, H. Rubin, and P. G. Winchell, The approximation of symmetric X-ray peaks by Pearson type VII distributions, J. Appl. Crystallogr. **10**, 66 (1977).
[30] E. P. Bellido, D. Rossouw, and G. A. Botton, Toward 10 meV electron energy-loss spectroscopy resolution for plasmonics, Microsc. Microanal. **20**, 767 (2014).
[31] S. Plimpton, Fast parallel algorithms for short-range molecular dynamics, J. Comput. Phys. **117**, 1 (1995).
[32] L. Lindsay and D. A. Broido, Optimized Tersoff and Brenner empirical potential parameters for lattice dynamics and phonon thermal transport in carbon nanotubes and graphene, Phys. Rev. B **81**, 205441 (2010).
[33] J. M. Dickey and A. Paskin, Computer Simulation of the Lattice Dynamics of Solids, Phys. Rev. **188**, 1407 (1969).
[34] E. Fransson, M. Slabanja, P. Erhart, and G. Wahnström, DYNASOR—A tool for extracting dynamical structure factors and current correlation functions from molecular dynamics simulations, Adv. Theory Simul. **4**, 2000240 (2021).
[35] A.-L. Hamon, J. Verbeeck, D. Schryvers, J. Benedikt, and R. M. C. M. v. d. Sanden, ELNES study of carbon K-edge spectra of plasma deposited carbon films, J. Mater. Chem. **14**, 2030 (2004).
[36] S. Korneychuk, G. Guzzinati, and J. Verbeeck, Measurement of the Indirect Band Gap of Diamond with EELS in STEM, Phys. Status Solidi A **215**, 1800318 (2018).
[37] A. Togo and I. Tanaka, First principles phonon calculations in materials science, Scr. Mater. **108**, 1 (2015).
[38] L. Shi, X. Ma, M. Li, Y. Zhong, L. Yang, W. Yin, and X. He, Molecular dynamics simulation of phonon thermal transport in nanotwinned diamond with a new optimized Tersoff potential, Phys. Chem. Chem. Phys. **23**, 8336 (2021).
[39] D. Takeuchi, H. Watanabe, S. Yamanaka, H. Okushi, H. Sawada, H. Ichinose, T. Sekiguchi, and K. Kajimura, Origin of band-Aemission in diamond thin films, Phys. Rev. B **63**, 245328 (2001).
[40] C. S. Granerod, W. Zhan, and O. Prytz, Automated approaches for band gap mapping in STEM-EELS, Ultramicroscopy **184**, 39 (2018).
[41] A. C. Ferrari and J. Robertson, Resonant Raman spectroscopy of disordered, amorphous, and diamondlike carbon, Phys. Rev. B **64**, 075414 (2001).
[42] R. Qi *et al.*, Measuring phonon dispersion at an interface, Nature (London) **599**, 399 (2021).
[43] L. Yang *et al.*, Suppressed thermal transport in silicon nanoribbons by inhomogeneous strain, Nature (London) **629**, 1021 (2024).
[44] K. D. Parrish, A. Jain, J. M. Larkin, W. A. Saidi, and A. J. H. McGaughey, Origins of thermal conductivity changes in strained crystals, Phys. Rev. B **90**, 235201 (2014).
[45] J. Lyu, S. Qiao, and L. Yang, Anisotropic heat conduction of silicon nanocube through strain gradient engineering, Nano Lett. **25**, 2988 (2025).
[46] G. Jiao, S. Qiao, J. Lyu, Y. Tao, and L. Yang, Suppression of thermal transport in bent boron arsenide nanoribbons, Phys. Rev. Appl. **22**, 054019 (2024).
[47] S. Qiao, Y. Tao, and L. Yang, Negative correlation between cross-plane bonding strength and in-plane thermal transport in bent van der Waals materials, Phys. Rev. B **110**, 245411 (2024).
[48] A. T. Collins, M. Kamo, and Y. Sato, Intrinsic and extrinsic cathodoluminescence from single-crystal diamonds grown by chemical vapour deposition, J. Phys. Condens. Matter **1**, 4029 (1989).
[49] G. C. Anderson, S. Prawer, P. Johnston, and D. McCulloch, The effect of carbon and nitrogen implantation on the abrasion resistance of type IIa (110) diamond, Nucl. Instrum. Methods Phys. Res., Sect. B **80–81**, 1451 (1993).
[50] J. Valendolf, J. C. Pinero, F. Lloret, G. Alba, D. Eon, and D. Araujo, Spectral and microstructural analysis of the effect of the Ga(+)implantation on diamond: a CL-EELS study, Nanotechnology **35**, 415701 (2024).
[51] J. Ruan, K. Kobashi, and W. J. Choyke, On the "band-A" emission and boron related luminescence in diamond, Appl. Phys. Lett. **60**, 3138 (1992).
[52] D. Araújo, M. P. Alegre, A. J. García, J. Navas, M. P. Villar, E. Bustarret, P. N. Volpe, and F. Omnès, Influence of the substrate type on CVD grown homoepitaxial diamond layer quality by cross sectional TEM and CL analysis, Diamond Relat. Mater. **20**, 428 (2011).
[53] J. F. Suyver, J. J. Kelly, and A. Meijerink, Temperature-induced line broadening, line narrowing and line shift in the luminescence of nanocrystalline ZnS:Mn2+, J. Lumin. **104**, 187 (2003).
[54] T. Hu *et al.*, Mechanism for Broadband White-Light Emission from Two-Dimensional (110) Hybrid Perovskites, J. Phys. Chem. Lett. **7**, 2258 (2016).
[55] Y. Zhang, S. Qiao, A. Lu, X. Sun, J. Lyu, J. Du, Y. Lu, and L. Yang, Figshare, Dataset for "Phonon-assisted broadband light emission in strain-gradient modulated diamond nanoribbons", 10.6084/m9.figshare.33111911 (2026).